ROYAL SOCIETY OF CHEMISTRY

PAPER

Effect of the Sr–Fe layered double hydroxide coating based on the microenvironment response on implant osseointegration in osteoporotic rats†

Chenyu Liao,[a] Dongcai He,[b] Kaiwen Yin,[a] Yuhung Lin, [ID][a] Yihan Chen, [ID][fg] Ziqiang Zhang,[b] Jing Zhang, [ID][e] Hongrong Luo,[d] Xianchun Chen*[c] and Yunfeng Li [ID]*[a]

Osteoporosis is a disease that manifests itself as an abnormality of bone metabolism and is characterized by low bone mass and destruction of the bone microstructure. Since bone resorption occurs more rapidly than new bone formation, osteoporosis leads to reduced orthopedic implant stability. From a microenvironmental point of view, the rationale for this outcome is that osteoclasts are overactive in the bone tissue of patients with osteoporosis, and the large amount of H^+ they produce leads to local chronic acidosis, which promotes bone mineral loss. Therefore, we designed a weakly alkaline layered double hydroxide (LDH) coating to modulate the pathologically acidic microenvironment and the osteogenic–osteoclastic coupling by releasing Sr^{2+}. We prepared Sr–Fe LDH coatings on pure titanium implants using a hydrothermal method in this study and characterized the material using SEM, AFM, XRD, XPS, EDS, ICP, pH acidimeter, *etc.* We found that the coatings had good nanomorphology and were able to efficiently neutralize H^+ as well as steadily release Sr^{2+} for up to 21 days. *In vitro*, the coating not only significantly promoted the adhesion, proliferation, and differentiation of osteoblasts, but also inhibited the differentiation of osteoclasts at the same time. In addition, in animal experiments, the coating significantly improved the mechanical stability of the implant in osteoporotic rats, increasing Sr–Fe LDH@Ti maximal push-out force by 72.2% compared to Ti. At the same time, the coating was effective in reversing the osteoporotic state, resulting in a 58.5% increase in BV/TV (%), and a 12.4% increase in Tb. N (1 mm^{-1}), a 31.6% increase in Tb. Th (μm), and a 30.9% increase in BA (%). Our results suggest that this Sr–Fe LDH nanocoating material with acid-neutralizing, as well as long-term Sr^{2+}-releasing capabilities, is a novel and effective orthopedic implant coating material under osteoporotic conditions.

[a] *State Key Laboratory of Oral Diseases & National Center for Stomatology & National Clinical Research Center for Oral Diseases & Department of Oral & Maxillofacial Surgery, West China Hospital of Stomatology, Sichuan University, Chengdu, 610041, China. E-mail: liyunfeng@scu.edu.cn*

[b] *College of Materials Science and Engineering, Sichuan University, No. 24 South Section 1, Yihuan Road, Chengdu, 610065, China*

[c] *College of Polymer Science and Engineering, Sichuan University, No. 24 South Section 1, Yihuan Road, Chengdu, 610065, China. E-mail: chenxianchun@scu.edu.cn*

[d] *College of Biomedical Engineering, Sichuan University, No. 24 South Section 1, Yihuan Road, Chengdu, 610065, China*

[e] *College of Architecture and Environment, Sichuan University, Chengdu, Sichuan 610065, China*

[f] *Shanghai Institute of Ceramics, Chinese Academy of Science, Research Unit of Nanocatalytic Medicine iSpecific Therapy for Serious Disease, Chinese Academy of Medical Sciences, Shanghai 200050, P.R. China*

[g] *Center of Materials Science and Optoelectronics Engineering, University of Chinese Academy of Sciences, Beijing 100049, P.R. China*

† Electronic supplementary information (ESI) available. See DOI: https://doi.org/10.1039/d3tb02410e

1. Introduction

Today, osteoporosis affects more than 1.02 billion people worldwide,[1] and the vast majority of these people are postmenopausal women and middle-aged and older men.[2] There is a very high demand for bone implants as these people are at high risk of tooth loss and bone joint diseases.[3]

It is well known that in osteoporotic patients, it is difficult to form enough bone to support the implant because of the osteogenic–osteoclastic uncoupling, which leads to loosening and detachment of the implant.[4–6]

In osteoporosis, the bone tissue microenvironment is characterized by reduced osteoblast activity and impaired bone tissue regeneration. In addition, hyperactive osteoclasts produce a slightly acidic environment by secreting large quantities of hydrogen ions, resulting in bone mineral loss and destruction of the bone microstructure. In addition, a high concentration of

1592 | *J. Mater. Chem. B*, 2024, **12**, 1592–1603

This journal is © The Royal Society of Chemistry 2024

H^+ will reduce osteoblast activity and inhibit bone tissue regeneration.[7–9] All of these factors affect bone metabolism and inhibit osseointegration, thereby increasing the risk of implant failure.[10] Therefore, in order to improve the osseointegration of implants, the coating material should not only focus on the modulation of cellular function but also on the modulation of the pathological acidic microenvironment.[11–13]

In order to modulate cellular function, many studies have been conducted to release growth factors such as bone morphogenetic proteins (BMPs), transforming growth factor-β (TGF-β), vascular endothelial growth factor (VEGF), interleukin-4 (IL-4), and interleukin-10 (IL-10) by constructing coatings on the implant surface that can be loaded with drugs.[14–18] However, these drugs, cytokines, or growth factors have disadvantages such as short half-life, susceptibility to inactivation, lack of long-term stability, tissue selectivity, potential toxicity, and dose-dependence,[19,20] making it difficult to achieve better results. The strategy of introducing strontium elements into coating materials and modifying pure titanium and titanium alloy implants to modulate cellular function is a strategy that is simple to prepare, inexpensive, and no less effective than strategies based on the release of drugs, cytokines, and growth factors and it has already produced impressive results. Coatings containing strontium can emit Sr^{2+} relatively steadily during in vivo degradation. Sr^{2+} is a known biologically active ion that, at appropriate concentrations,[21–23] increases pro-osteoblast activity and inhibits osteoclast overactivity, thereby regulating bone metabolism and promoting osseointegration.[24–28]

Layered double hydroxide (LDH), a biomaterial composed of a body laminate of divalent and trivalent cations and a guest laminate of anions, has been investigated extensively in the field of bone repair.[29,30] The formula for this substance is $[M_{1-x}^{2+}N_x^{3+}(OH)_2]^{x+}[An_{x/n}^{n-}]^{x-} \cdot mH_2O$. LDH's chemical composition is modifiable, and various biological effects can be conferred on LDH by introducing different bioactive elements.[31,32] Notably, LDH is an alkaline substance, and its first biomedical application was as a pH-raising anti-acid medication. LDH has an acidic environmental response, and LDH coatings containing bioactive elements can undergo an acid-neutralization reaction with H^+ in acidic environments and degrade swiftly, releasing bioactive ions. In contrast, it self-degrades slowly in neutral and alkaline environments.[33,34]

Therefore, in order to regulate the abnormal acidic microenvironment of osteoporosis, as well as to improve the dysfunctional state of osteoblasts and osteoclasts, and ultimately to enhance osteointegration, we combined the excellent performance of Sr^{2+} in improving bone metabolism in this work with the ability of alkaline LDH to neutralize acid and utilized the biologically-safe Fe^{3+} to assist in the construction of the Sr–Fe LDH coating. To verify that this was achieved, we used ICP to measure the ability of Sr^{2+} to be released in PBS and a pH acidimeter to detect the ability of Sr–Fe LDH to neutralize H^+. The effects of Sr–Fe LDH coating on the function of osteoblasts and osteoclasts were investigated using mouse embryonic osteoblasts (3T3-E1) and mouse monocyte macrophage leukemia cells (RAW264.7) as cell models. The effect of Sr–Fe LDH coating on osseointegration was investigated using ovariectomized rats as a model. Our results show that the Sr–Fe LDH coating can release Sr^{2+} for a long time and stably, and has a good acid-neutralising ability. In vitro, it can significantly promote the proliferation and differentiation of osteoblasts while inhibiting the differentiation of osteoclasts. In addition, the Sr–Fe LDH coating was able to improve the mechanical stability, peripheral bone formation, and osseointegration of implants in vivo.

2. Methods

2.1 Preparation of materials

The pure titanium size used for in vitro experiments in this study was 10 mm × 1 mm and the bar implant size used for in vivo experiments was 10 mm × 1 mm. The surface of pure titanium was ground, polished, and then acid etched for 90 s using 0.2 vol% hydrofluoric acid. We used the most widely used and simple hydrothermal method for the preparation of Sr–Fe LDH: firstly, 4.008 g of sodium hydroxide was added to the PTFE liner with 60 ml of deionised water, and mechanically stirred completely and allowed to dissolve, then pure titanium flakes or rods were added, followed by the addition of 1.5899 g of sodium carbonate, 6.2172 g of strontium oxide, and 6.4122 g of ferric hydroxide, in that order. Stirring was continued for 30 min. Finally, the PTFE liner was placed in a hydrothermal kettle and the hydrothermal reaction was carried out at a temperature of 120 °C for 14 h. To remove the residual impurities, the prepared material was required to be ultrasonically cleaned with 50% ethanol more than 5 times. In this work, we refer to pure titanium sheets and pure titanium implants as Ti, and to sheets and implants prepared with Sr–Fe LDH coatings as Sr–Fe LDH@Ti.

2.2 Characterization of materials

A field emission scanning electron microscopy (FE-SEM, Apreo 2 S Lovac, Czech Republic) and an atomic force microscope (AFM, SPM-9600, Japan) were used to investigate the surface morphology and the roughness of the samples. The crystal structure of the samples was examined via X-ray diffraction (XRD). X-ray photoelectron spectroscopy (XPS) was used to analyze the elemental composition and chemical state of the samples. The thickness, elemental species, and elemental distribution of the samples were detected using X-ray energy spectrometry (EDS). The hydrophilicity of the materials was analyzed using an optical contact angle meter (DSA25E, DEU). Sr^{2+}, which has a bone repair regulatory function, was quantified using inductively coupled plasma emission spectroscopy (ICP-OES). Analysis of the acid-neutralizing capacity of samples using a pH acidimeter.

2.3 In vitro study

2.3.1 Cell culture. The medium for MC3T3-E1 cells should consist of 89% α-MEM (Gibco, USA) plus 1% penicillin/streptomycin (Hyclone, USA) and 10% FBS (Gibco, Australia). The medium

This journal is © The Royal Society of Chemistry 2024

J. Mater. Chem. B, 2024, 12, 1592–1603 | 1593

components for RAW264.7 cells should consist of 89% DMEM (Gibco, USA) + 1% penicillin/streptomycin (Hyclone, USA) + 10% FBS (Gibco, AUS). Both cell types were cultured in 6 cm Petri dishes (NEST, CHA) and a CO_2 incubator (37 °C, 5% CO_2, and 90% relative humidity, SERIES II WATER HACKET, USA). Every 2–3 days, the cells were washed with PBS and the medium was replaced with the new medium. When 80–90% of the cells were fused, they had to be passed at a ratio of 1:3 or 1:4.

2.3.2 Cell adhesion and morphology. 500 ml of MC3T3-E1 and RAW264.7 cell suspensions were configured at densities of 1×10^4 cells per ml and 2×10^4 cells per ml, respectively, and then the cells were inoculated onto the surface of the material placed in a 48-well plate, which was then placed in a cell-specific culture incubator at 37 °C for 24 hours. After 24 hours, the cells were rinsed twice with PBS and then fixed for 24 hours with an electron microscope fixative (Service bio, CHN). After 24 hours, a 15 minute gradient dehydration was performed using 30%, 50%, 70%, 85%, 95%, and 100% ethanol. After drying and conductive treatment, the cells were ultimately observed using a scanning electron microscope (JSM-6510LV, JPN).

Method for laser confocal microscopy observation: 500 ml of MC3T3-E1 and RAW264.7 cell suspensions were prepared at a density of 1×10^4 cells per ml and 2×10^4 cells per ml, respectively. The cells were then inoculated onto the surface of the material and placed in 48-well plates, which were then placed in a cell-specific culture incubator at 37 °C for 24 hours. After twenty-four hours, the cells were rinsed twice with PBS and then incubated at room temperature. After two washes, the cells were sequentially fixed with 4% paraformaldehyde, permeabilized with 0.2% Triton X-100, and stained at room temperature with YF®/rhodamine-labelled ghost pen cyclic peptide (Uelandy, CHN) and DAPI (Biosharp, CHN) for the cell membrane and nucleus, respectively. Observations were carried out using a laser confocal microscope (Olympus SpinSR10, Japan).

2.3.3 Cytocompatibility evaluation. The biocompatibility of the materials with MC3T3-E1 and RAW264.7 was evaluated by live and dead cell fluorescence staining: 500 µl of cell suspension was configured at a density of 4×10^4 cells per ml and 8×10^4 cells per ml, respectively, and then the cells were inoculated onto the surface of the materials in a 48-well plate and co-cultured with the materials. Live and dead cells were fluorescently stained with a calcein/PI cell activity and cytotoxicity detection kit (beyotime, CHN) and then observed with an orthogonal fluorescence microscope (Leica DM4 B, DEU) following 24 h of incubation at 37 °C in a cell-specific incubator.

The CCK8 method was used to determine the effect of the materials on the cell viability of MC3T3-E1 and RAW264. 7: 500 µl of the cell suspension was configured at a density of 1×10^4 cells per ml and 2×10^4 cells per ml, respectively, and then the cells were inoculated on the surface of the materials placed in a 48-well plate and co-cultured with the materials for 1, 3, and 5 days. Every two days, the medium was substituted with the new medium. After 2 thorough washes with 500 ml of PBS (biosharp, CHN) on 1, 3, and 5 days, 200 µl of 10% CCK8 solution (Biosharp, CHN) freshly configured with the culture medium was added to each well. The absorbance was measured at 450 nm using an enzyme marker (Synergy H1, USA) following a 2 hour incubation at 37 °C in a cell-specific incubator.

2.3.4 Osteogenic differentiation experiments. First, sodium-glycerophosphate, dexamethasone, and vitamin C were added to -DMEM until their final concentrations were 10 mM, 0.1 M, and 50 µg ml^{-1}, respectively.

Method for ALP staining: 500 µl of the MC3T3-E1 cell suspension with a density of 4×10^4 cells per ml was inoculated onto the surface of both materials in 48-well plates, respectively, and the new induction solution was replaced every 2 days. Following a 7 day incubation at 37 °C in a cell-specific incubator, the cells were rinsed twice with PBS and fixed with 4% paraformaldehyde. The cells were stained with a BCIP/NBT alkaline phosphatase chromogenic reagent (Beyotime, CHN) for 24 hours at room temperature. After adding 200 µl of DMSO to each well and stirring for 30 minutes to dissolve the blue alkaline phosphatase crystals, 100 µl of the solution was aspirated, and the absorbance was measured at 520 nm using an enzyme marker.

ARS staining method: 500 µl of the MC3T3-E1 cell suspension with a density of 4×10^4 cells per ml was inoculated onto the surface of both materials placed in 48-well plates, respectively, and the new induction solution was replaced every 2 days. After 21 days of incubation at 37 °C in a cell-specific incubator, the cells were twice rinsed with PBS and then fixed with 4% paraformaldehyde. The cells were then stained for 24 hours at room temperature with 1% alizarin red solution (Solarbio, CHN). Finally, 200 µl of 10% cetylpyridinium chloride solution was added to each well, agitated for 30 minutes, and 100 µl of the solution was aspirated and analyzed using an enzyme marker for absorbance at 562 nm.

2.3.5 Osteoclastic differentiation experiments. Configuration of extraction solution: by the ISO 10993-12 standard 3 cm^2 ml^{-1} extraction ratio, the material was co-cultured with the osteoblast differentiation medium for 24 hours. After 24 hours, the extraction solution was collected and refrigerated at 4 °C for future experiments.

TRAP staining procedure: RAW264.7 cells were seeded at a density of 6000 cells per cm^2 in 48-well plates, and the induction solution was replaced every two days. After 6 days of induction, the cells were rinsed twice with PBS and successively permeabilized with 4% paraformaldehyde fixation and 0.2% Triton-X 100. The cells were then stained for 1 hour with a TRAP staining reagent (Servicebio, CHN) and observed under a light microscope.

RAW264.7 cells were seeded onto the surface of the material in 48-well plates at a density of 6000 cells per cm^2, and the induction solution was replaced every two days. After 6 days of induction, the cells were washed twice with PBS, fixed with 4% paraformalde, permeabilized with 0.2% Triton-X 100, and stained with YF®/rhodamine-labelled phantom pen cyclopeptide and DAPI, respectively, for cell membrane and nucleus. Lastly, laser confocal microscopy was utilized for observation purposes.

6000 cells per cm^2 RAW264.7 were seeded onto the surface of the material in 48-well plates for RT-qPCR, and the induction

1594 | J. Mater. Chem. B, 2024, 12, 1592–1603

This journal is © The Royal Society of Chemistry 2024

solution was replaced every two days. After incubation for six days, the plate was rinsed twice with PBS. RNA was extracted using the RNAiso Plus kit. The relative expression of osteoblast-associated genes NFATc1, c-FOS, CTSK, and TRAP was determined using a real-time fluorescence quantitative PCR instrument (Bio-rad CFX96 Touch, USA) and -actin as an internal reference gene.

2.4 *In vivo* study

2.4.1 Anaesthesia and surgery on animals. Three-month-old female Sprague-Dawley rats weighing 200–250 g were selected. The rearing conditions were 25 degrees Celsius, 55 percent humidity, and 12 hours of light followed by 12 hours of darkness. The rodents were permitted to consume food and water at will. Animal experiments were conducted in precise accordance with the Sichuan University Animal Protection Committee-approved ARRIVE guidelines.

Regarding the method of anesthesia: we anesthetized the animals three times in our animal experiments: the osteoporosis model establishment experiments, the implant placement experiments, and at the time of animal execution. We anesthetized the rats by intraperitoneal injection of 3% sodium pentobarbital solution (45 mg kg^{-1}). At the same time, 2% lidocaine was used for local infiltration anesthesia within the incision area to achieve the best anesthesia effect.

Regarding the method of execution: we euthanized the animals by injecting an overdose of 3% pentobarbital sodium solution (150 mg kg^{-1}) into the peritoneal cavity of SD rats.

Ti and Sr–Fe LDH@Ti were implanted into the bone marrow compartments of the bilateral tibiae of rats in both groups parallel to the long axis of the tibiae and slightly below the articular surface twelve weeks after bilateral ovariectomy. All rodents received intramuscular antibiotics and analgesics for three days following surgery. After 8 W of implant placement, all rodents were euthanized, and specimens were collected for further study.

2.4.2 Biomechanical test. The end of the implant was exposed by epiphysis separating the left tibia of the rodent. The samples were embedded with the self-coagulating resin so that the implant could be moved perpendicular to the carrier table from the bone marrow cavity. For egress testing of these samples, an electronic universal material testing machine (INSTRON5565, USA) was used. The compression rate was set to 1 mm min^{-1}, the displacement *versus* force relationship was recorded, and the maximal push-out force was determined.

2.4.3 Micro-CT evaluation. After collecting the samples, they were fixed with 4% paraformaldehyde for 48 hours before being scanned with a micro-computed tomography scanner (Micro-CT 100, CH). The system was set to 70 kV, 200 A, 10 m per layer for the tibia and 90 kV, 200 A, 10 µm per layer for the implants. To reduce the effect of noise, the Gaussian filter parameters were set to = 1.2, support = 1. In the tibia investigation, the region of interest (VOI) was positioned 100 layers beneath the growth plate within the bone marrow. In implant analysis, the region of interest (VOI) was established within a ring 500 µm from the implant surface with a total of one thousand layers (10 000 µm). The VOI region was evaluated for bone volume fraction (BV/TV), trabecular thickness (Tb. Th), trabecular number (Tb. N), trabecular separation (Tb. Sp), and bone-implant contact (BIC).

2.4.4 Histomorphometric analysis. Immediately following micro-CT, implant-bearing samples were dehydrated with an ethanol gradient, infiltrated with resin, and photocured with methyl isocrotonate. The segment was cut using a microtome for hard tissue (EXAKT300CP, DEU). The obtained slices' ultimate thickness is 60 µm after grinding and polishing with a grinding machine (EXAKT400CS, DEU). The region of interest, stained with 1% toluidine blue and extending 100 µm from the implant's surface, was defined as a ring area. The percentage of bone tissue area (BA) in the region of interest was quantified using the Leica DMI 6000B microscope and its software. After the rats were killed, their five organs were promptly preserved in 4% paraformaldehyde and fixed for 48 hours, followed by gradient dehydration, pruning, embedding, slicing, hematoxylin–eosin staining, and sealing.

2.5 Statistical analysis

All data were expressed as mean ± standard deviation and statistically analyzed using IBM SPSS Statistics 26 software (SPSS, 14hicago, IL, USA). Comparisons between groups were made using the independent samples *t*-test. $p < 0.05$ was considered statistically significant.

3. Result and discussion

3.1 Synthesis and characterization of the Sr–Fe LDH coating

Scanning electron microscopy (Fig. 1A) and atomic force microscopy (Fig. 1B and Fig. S1A, ESI†) were utilized to observe the morphology of the samples, and uniform nanospherical Sr–Fe LDHs were found on the surface of pure titanium but there is no significant difference in roughness between Ti and Sr–Fe LDH@Ti (Fig. S1B, ESI†). We then conducted XRD and XPS analyses. In the XRD mapping characterization of Ti and Sr–Fe LDH@Ti (Fig. 1C), it can be seen that Sr–Fe LDH@Ti, in addition to the diffraction peaks of Ti, diffraction peaks are also detected at around 10° and 20°, corresponding to the (0 0 3) and (0 0 6) crystal planes, which are consistent with the typical LDH physical structure (PDF# 50-0652). From the XRD patterns (Fig. S2, ESI†), we can observe that the Sr–Fe LDH powders are mainly composed of two main phases, namely $Sr_3Fe_2OH_{12}$ and FeOOH. The diffraction peaks of these phases exhibit sharp and symmetric features, which is a typical sign of the integrity and crystallinity of the crystal structure. This means that during the synthesis of Sr–Fe LDH, both phases formed a structure with excellent crystallinity, and it can also prove that the synthesis of Sr–Fe LDH was successful. XPS spectroscopy analysis was performed to further ascertain the surface elemental states of the coatings, the Ti, Fe, Sr, C, and O elements were observed in the complete XPS spectra of the sample surface (Fig. 1D). A split-peak fitting procedure was performed on the Fe 2p binding energy peaks (Fig. 1E), and it
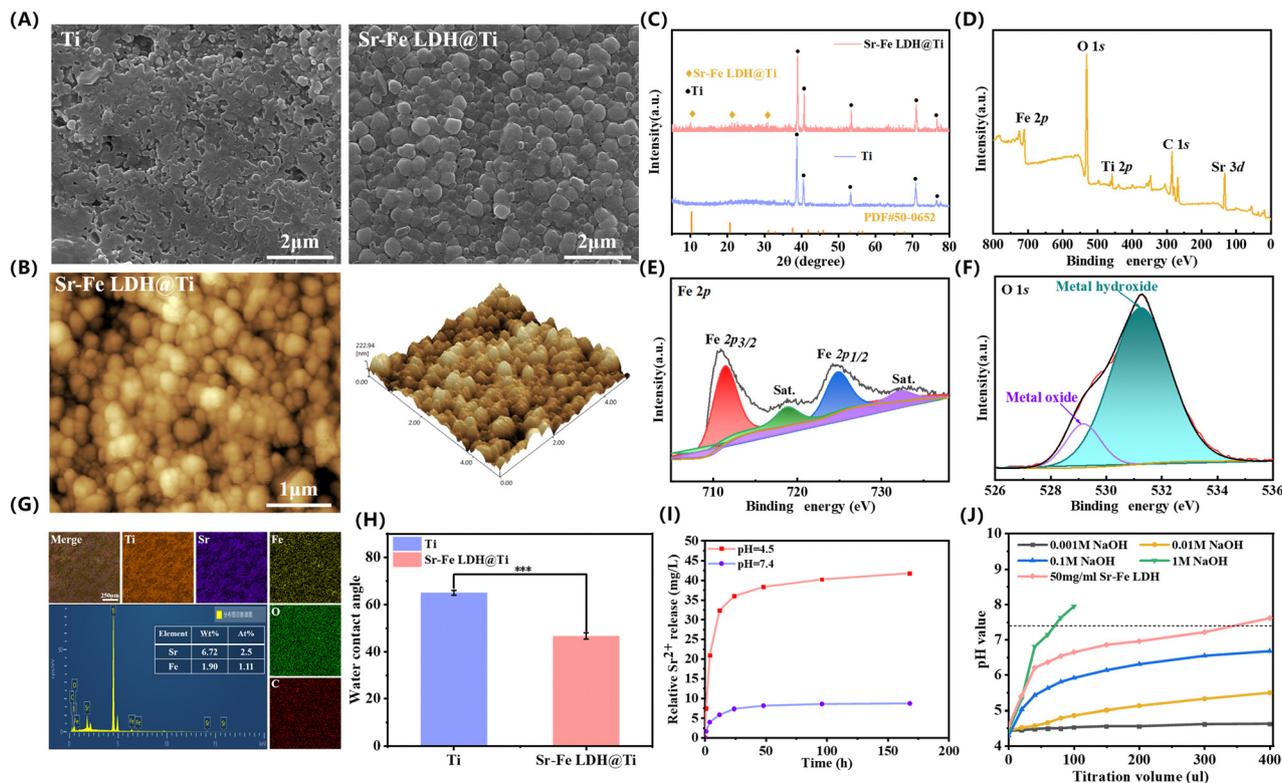
This journal is © The Royal Society of Chemistry 2024

J. Mater. Chem. B, 2024, **12**, 1592–1603 | 1595

Fig. 1 (A) SEM images of Ti and Sr–Fe LDH@Ti. (B) AFM images and quantitative analysis of Sr–Fe LDH@Ti; (C) XRD images of Ti and Sr–Fe LDH@Ti. (D) Complete XPS spectrum images of Sr–Fe LDH@Ti. (E) Split-peak fitting of the Fe 2p binding energy peaks of Sr–Fe LDH@Ti. (F) O 1s split peak fitting images of Sr–Fe LDH@Ti. (G) Elemental analyses of Sr–Fe LDH@Ti by EDS. (H) Analyses of contact angle test of Ti and Sr–Fe LDH@Ti; n = 6. (I) The release curves of Sr^{2+} ions from Sr–Fe LDH@Ti. (J) pH-value monitoring during the titration of Sr–Fe LDHs and NaOH into acidic PBS (pH = 4.5). All values are presented as mean ± s.d. *$p < 0.05$, **$p < 0.01$, and ***$p < 0.001$.

can be seen that the peaks at 714.5 eV and 724.8 eV represent the peaks of Fe $2p_{3/2}$ and Fe $2p_{1/2}$, whereas the binding energy peaks at 718.3 eV and 732.4 eV are satellite peaks of Fe $2p_{3/2}$ and Fe $2p_{1/2}$. This indicates the presence of both Fe^{2+} and Fe^{3+} in Sr–Fe LDH. It indicates that Sr–Fe LDH contains both Fe^{2+} and Fe^{3+}. The results of the O 1s split peak fitting (Fig. 1F) reveal that the two peaks appearing at 529.1 and 531.2 eV correspond to metal oxides and metal hydroxides, respectively, and the ratio of the half-peak widths of the two peaks is close to 1 : 6, indicating that the majority of the elemental oxygen exists in the form of metal hydroxides. EDS (Fig. 1G) revealed that Sr, Fe, O, and C are uniformly distributed on the surface of pure titanium and Sr^{2+} of 6.72% weight percent (wt%) and 2.5% atomic percent (at%). Combining SEM and EDS analyses, we found that the thickness of the coating was 2.1 μm (Fig. S3, ESI†). Hydrophilicity is an important factor affecting the surface activity of implants, and the majority of studies[35,36] have concluded that hydrophilic surfaces are preferable to hydrophobic surfaces for promoting early cell proliferation and osteogenic differentiation. Consequently, we employed the seated drop method for contact angle analysis of Ti and Sr–Fe LDH@Ti (Fig. 1H), and the result demonstrates that Sr–Fe LDH@Ti is more hydrophilic than Ti. Sr^{2+} is believed to promote osteoblast differentiation while inhibiting osteoclast differentiation,[37,38] so to verify the degradation ability of the

Sr–Fe LDH coating, we used inductively coupled plasma emission spectrometry (ICP) to quantify the Sr^{2+} released from Sr–Fe LDH@Ti in PBS buffer at a specific time. Quantitative analysis of Sr^{2+} in the medium at specific times by inductively plasma emission spectroscopy (ICP) (Fig. 1I) showed that Sr^{2+} was released at a high rate during 2 days, and then gradually reached the ion release equilibrium, which allowed Sr^{2+} to be released slowly. Among them, the Sr^{2+} release concentration of Sr–Fe LDH@Ti in pH = 4.5 PBS within 2 days was 38.3 mg L^{-1}, while that at pH = 7.4 PBS was 8.05 mg L^{-1}. Analyses by EDS showed that the content of Sr on the surface of the material after 7 days of immersion in pH = 4.5 solution was significantly lower than that in pH = 7.4 solution (Fig. S4, ESI†). The higher degradation rate in acidic PBS compared with that in neutral PBS illustrated the sensitive and efficient response of Sr–Fe LDH@Ti to the acidic environment. More importantly, Sr^{2+} could be slowly released in PBS at pH = 7.4 for up to 21 days (Fig. S5, ESI†), indicating that Sr–Fe LDH@Ti could slowly release Sr^{2+} for a long period, which is important for the long-term regulation of the local pathological microenvironment in osteoporosis. In the pathological microenvironment of osteoporosis, mature and functionally active osteoclasts secrete large amounts of H^+ on the bone surface, leading to the dissolution of hydroxyapatite, the main inorganic component of bone tissue, and can promote the degradation of organic

1596 | J. Mater. Chem. B, 2024, 12, 1592–1603

This journal is © The Royal Society of Chemistry 2024

components by histaminase K (CTSK) and anti-tartaric acid phosphatase (TRAP).[39] At the same time, large amounts of H^+ negatively affect calcium salt deposition and mineralization of the bone-like material. From the point of view of the cell itself, excess H^+ can have a great impact on osteoclast function, mainly in the form of increased expression of genes that promote bone resorption function, including carbonic anhydrase II,[40] calcitonin receptor, tissue protease K (CTSK), and tartrate-resistant acid phosphatase (TRAP). Notably, since H^+ is supplied by carbonic anhydrase II from osteoblasts, the low pH

microenvironment prompts osteoblasts to secrete more H^+, thus creating a vicious cycle that promotes bone resorption.[41] For osteoblasts, excess H^+ down-regulates the expression of osteogenesis-related genes, so it is important for materials to have good acid-neutralizing properties to inhibit bone resorption.[7,34] Since Sr–Fe LDH is an alkaline material, we speculate that it can be degraded while neutralizing H^+. To verify our conjecture, we formulated 50 mg ml^{-1} pulverized Sr–Fe LDH with purified water and compared it to gradients of NaOH concentration (Fig. 1J). It can be observed that its acid
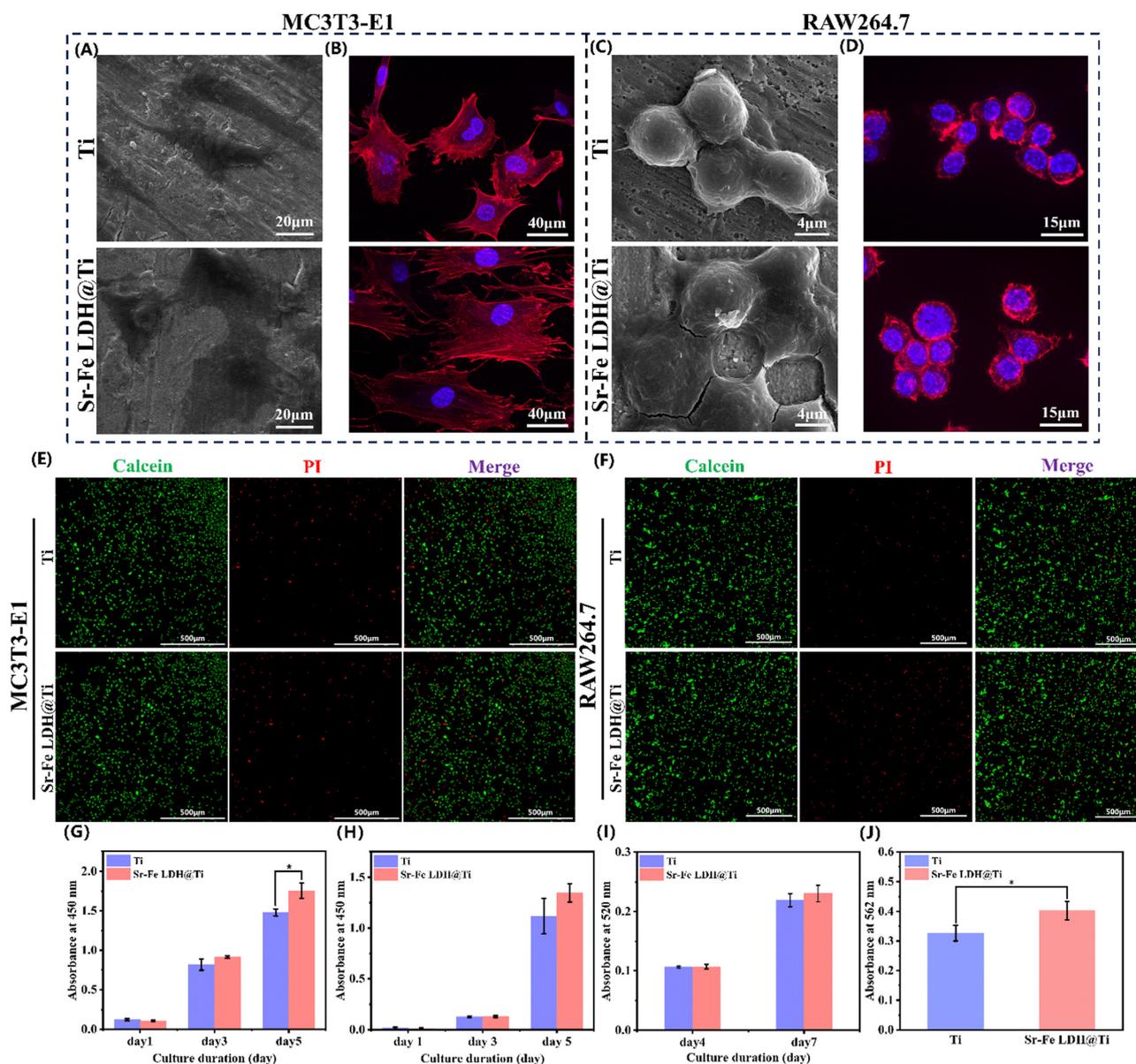

Fig. 2 (A) SEM images of MC3T3-E1 cultured with Ti and Sr–Fe LDH@Ti for 24 h. (B) Confocal laser microscopy images of MC3T3-E1 costained with rhodamine–phalloidin (red) and DAPI (blue) on the surface of Ti and Sr–Fe LDH@Ti. (C) SEM images of RAW264.7 cultured with Ti and Sr–Fe LDH@Ti for 24 h. (D) Confocal laser microscopy images of RAW265.7 are combined with rhodamine–phalloidin (red) and DAPI (blue) on the surface of Ti and Sr–Fe LDH@Ti. (E) and (F) Fluorescence staining images of MC3T3-E1 and RAW264.7 with Calcein-AM/PI after coculture on the surface of different materials for 24 h. CCK8 test of MC3T3-E1 (G) and RAW264.7 (H) Cultured with Ti and Sr–Fe LDH@Ti; $n = 3$. Analysis of (I) ALP staining and (J) alizarin red staining of the MC3T3-E1 treated with Ti and Sr–Fe LDH@Ti scaffolds at days 21 and 7, respectively; $n = 3$. All values are presented as mean ± s.d. $*p < 0.05$, $**p < 0.01$, and $***p < 0.001$.

This journal is © The Royal Society of Chemistry 2024

J. Mater. Chem. B, 2024, **12**, 1592–1603 | **1597**

neutralization ability is between 0.1 M and 1 M NaOH, which is a strong indication of its excellent acid neutralization ability.

3.2 *In vitro* study

3.2.1 Sr–Fe LDH@Ti promotes the adhesion and spread of MC3T3-E1 and RAW264.7. Observing the proliferation of cells on the material's surface is essential for determining its biocompatibility.[42] To determine the effect of Sr–Fe LDH coating on the adhesion and morphology of MC3T3-E1 and RAW264.7 cells, the two cell types were seeded for 24 hours on the surfaces of Ti and Sr–Fe LDH@Ti, respectively. The cells were then observed using scanning electron microscopy. As shown, MC3T3-E1 (Fig. 2A and B) and RAW264.7 (Fig. 2C and 2D) extended more pseudopods and expanded out over a larger area on the Sr–Fe LDH-coated surface of the material. This is probably because, during cell adhesion, the host cell does not interact directly with the surface of the material, but with the protein. Proteins in the extracellular matrix mediate cell adhesion by coupling to the cell contractile actin cytoskeleton *via* integrin receptors. It has been shown that increasing the hydrophilicity of the material can significantly increase the adsorption of proteins on the surface of the material and thus promote cell adhesion, thus Sr–Fe LDH@Ti with better hydrophilicity plays a

better role than Ti in promoting cell adhesion and spread,[43] establishing a solid foundation for the cells to carry out other biological functions.[44]

3.2.2 Sr–Fe LDH@Ti has good biosafety for MC3T3-E1 and RAW264.7. The effects of the substances on osteoblasts, osteoclast precursor cells, and immune cells were examined. As study subjects, we selected the most extensively used mouse embryonic osteoblast precursor cells (MC3T3-E1) and mouse monocyte macrophage leukemia cells (RAW264.7).[38,45,46] Biosafety is one of the most important factors in determining whether an implant can be clinically implemented, so we analyzed the biosafety of the Sr–Fe LDH coating first. MC3T3-E1 and RAW264.7 cells were seeded onto the Ti and Sr–Fe LDH@Ti surfaces, and after 24 h of resting, the calcein/PI cell activity and cytotoxicity detection kits were used to stain the living and dead cells on the surfaces of the materials. As shown in the figure (Fig. 2E and F), green fluorescence was observed in large numbers on both Ti and Sr–Fe LDH, indicating that the substantial majority of MC3T3-E1 and RAW264.7 cells were viable. Few cells were stained with red fluorescence, indicating that they were already deceased, while almost no cells were stained with yellow fluorescence, indicating that they were undergoing apoptosis. For additional quantitative analysis, we seeded MC3T3-E1 and RAW264.7 cells on
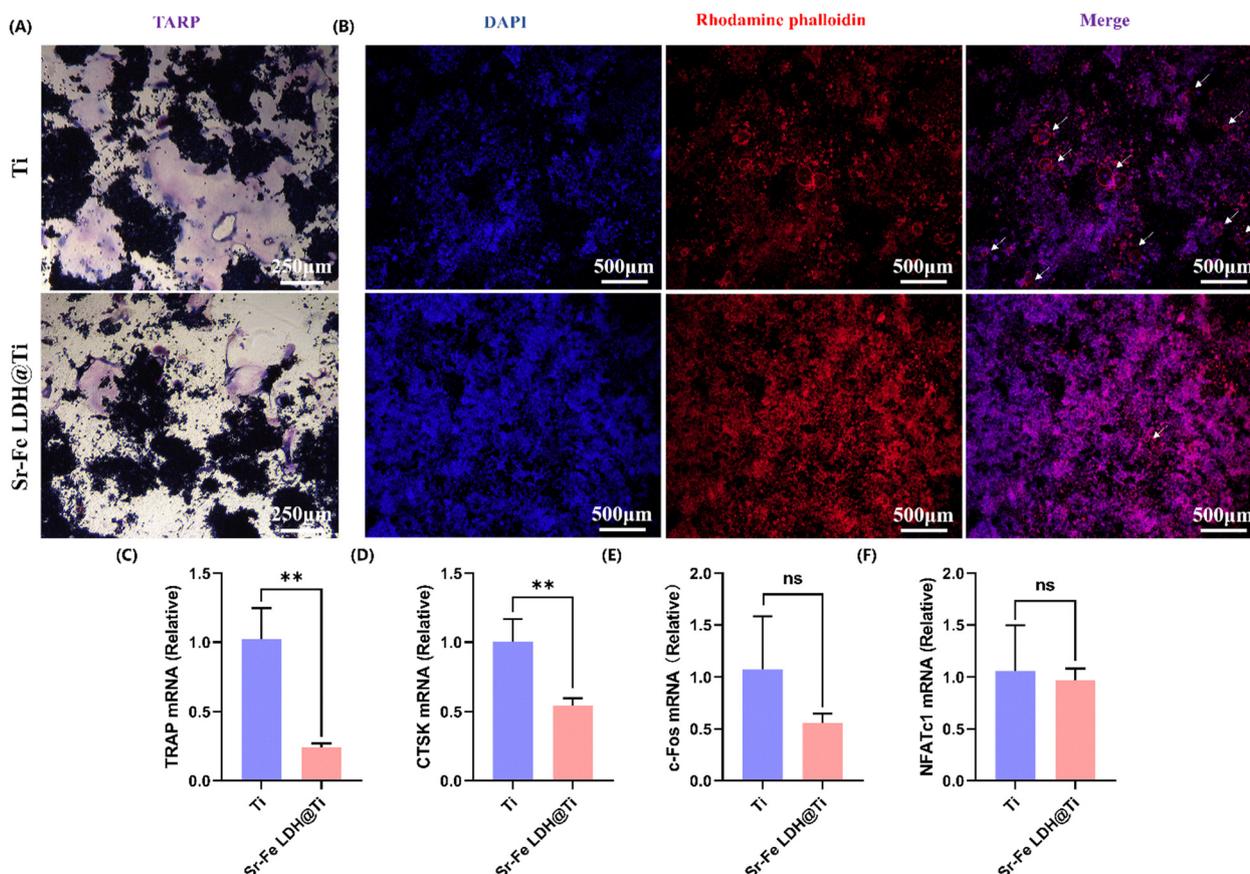

Fig. 3 (A) TRAP staining images of RAW264.7 cultured with Ti and Sr–Fe LDH@Ti extract in the presence of RANKL (50 ng ml^{-1}) for 6 days. (B) Confocal laser microscopy images of osteoclasts costained with anti-vinculin (green), rhodamine phalloidin (red), and DAPI (blue). (C)–(F) The qRT-PCR results of the expression of osteoclast marker genes including TRAP, CTSK, c-Fos, and NFATc1. All values are presented as mean ± s.d. *$p < 0.05$, **$p < 0.01$, and ***$p < 0.001$; $n = 3$.

1598 | *J. Mater. Chem. B*, 2024, **12**, 1592–1603

This journal is © The Royal Society of Chemistry 2024

the Ti and Sr–Fe LDH surfaces, respectively, and measured their proliferation using a CCK8 assay reagent. As shown, there was no significant difference in the proliferation status of MC3T3-E1 cells after 1 and 3 days of growth on Ti and Sr–Fe LDH@Ti, respectively, but MC3T3-E1 cells proliferated better after 5 days of growth on Sr–Fe LDH@Ti than on Ti (Fig. 2G), a phenomenon that is most likely to be the result of the sustained release of Sr^{2+} that has the effect of promoting cell proliferation.[47] RAW264.7 cells were grown on Ti and Sr–Fe LDH@Ti for 1, 3 and 5 days, respectively, and there was no significant difference in proliferation status (Fig. 2H). These findings suggest that the Sr–Fe LDH coating is biologically safe. These findings suggest that the Sr–Fe LDH coating is biologically safe. Green fluorescence was observed on both Ti and Sr–Fe LDH, indicating that the substantial majority of MC3T3-E1 and RAW264.7 cells were viable. Few cells were stained with red fluorescence, indicating that they were already dead, while almost no cells were stained with yellow fluorescence, indicating that they were undergoing apoptosis.

3.2.3 Sr–Fe LDH@Ti promotes differentiation and mineralization of MC3T3-E1. It is well established that ALP is an early marker of osteogenic differentiation and that the quantity of

calcium nodule deposition in the ECM is a late marker.[48,49] To verify the effect of Sr–Fe LDH coating on the osteogenic differentiation of osteoblasts, we employed them as a criterion for assessing osteogenic differentiation in this study. The semi-quantitative results of the BCIP/NBT method by ALP staining (Fig. 2I) indicated that Ti and LDH@Ti did not affect the early osteogenic differentiation of MC3T3-E1. However, the semi-quantitative results of the analysis by alizarin red staining (ARS) (Fig. 2J) indicated that Sr–Fe LDH significantly promoted the late osteogenic differentiation of MC3T3-E1 ($p < 0.05$). Therefore, it can be shown that our material enhances the cellular production of mineralized matrix. Since osteoblasts in osteoporosis patients suffer from a reduced ability to form and mineralize bone matrix,[50] the function exhibited by our material has the potential to reverse this pathological state.

3.2.4 Sr–Fe LDH@Ti inhibited RANKL-mediated osteoclastic differentiation. RAW264.7 is an osteoclast precursor cell; therefore, we used it as an osteoclast precursor cell in this investigation. As shown in Fig. 1, we first investigated the effect of the auto-degradation products of Sr–Fe LDH coating on osteoclast differentiation. The Sr–Fe LDH extract significantly
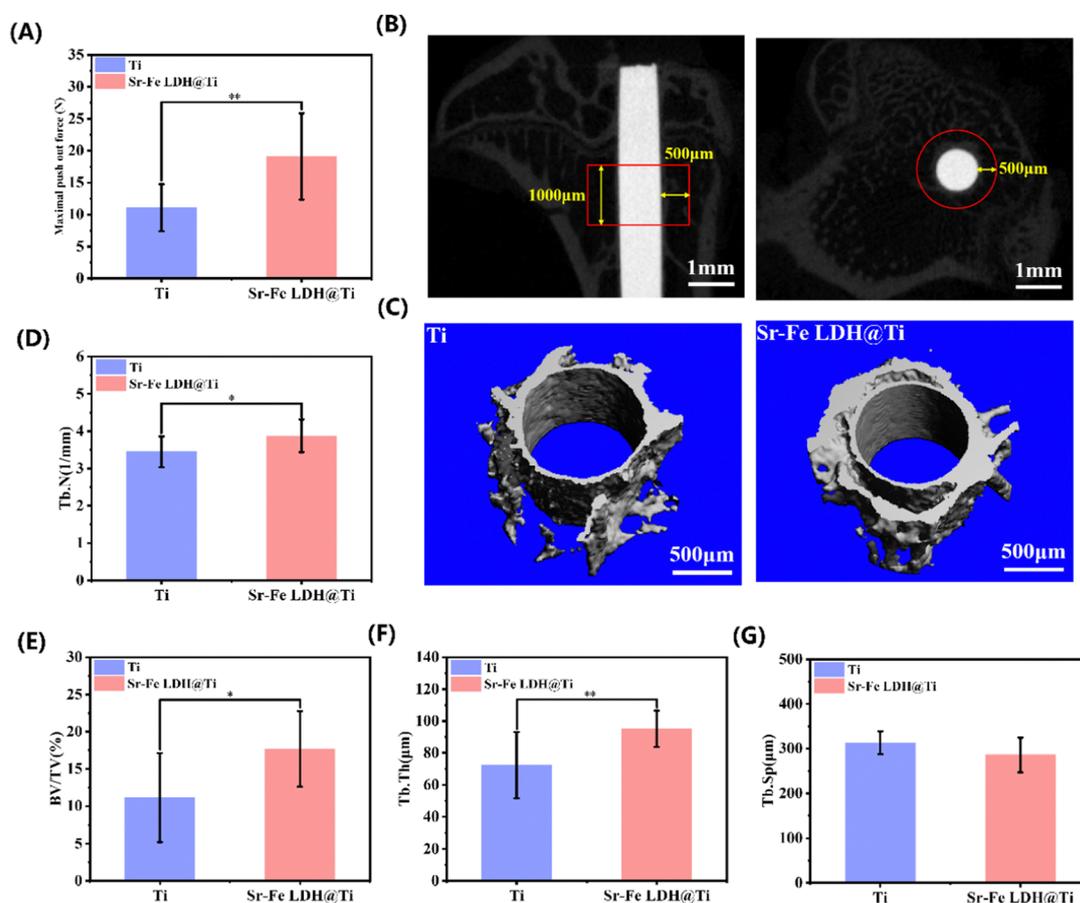

Fig. 4 (A) Quantitative results of the biomechanical test of implant fixation 8w after implant insertion, presented as the maximal push-out force; $n = 9$. (B) X-ray illustration of implant implantation and VOI. (C) Three-dimensional micro-CT images of the bone tissue around Ti and Sr–Fe LDH@Ti implants in the volume of interest (VOI). (D)–(G) Quantitative results of the micro-CT evaluation of implant osseointegration and trabecular microstructure around implants within the volume of interest; $n = 11$. All values are presented as mean $\pm$ s.d. *$p < 0.05$, **$p < 0.01$, and ***$p < 0.001$.

This journal is © The Royal Society of Chemistry 2024

J. Mater. Chem. B, 2024, **12**, 1592–1603 | **1599**

inhibited the formation of osteoclasts compared to Ti, and we can see the cell area and quantity of TRAP-positive osteoclasts were considerably reduced (Fig. 3A). This is likely due to the degradation of the Sr–Fe LDH coating, which increased the Sr^{2+} concentration. To determine whether acid neutralization of Sr–Fe LDH coating has a synergistic effect on inhibiting osteoclast differentiation in the presence of direct cell contact, we inoculated the cells on the surface of the two materials, bearing in mind that the surface pH value and ion concentration of the material are significantly higher than in other parts of the solvent.[51] Using confocal laser microscopy, the cell nucleus and cell membrane were fluorescently stained and observed (Fig. 3B). On the surface of Ti, a substantial number of cells with the characteristic multinucleated giant cell morphology of osteoclasts are visible, whereas these cells are rare on Sr–Fe LDH. qRT-PCR was used to detect the expression of genes involved in osteoclastic differentiation. CTSK gene expression decreased by 45.8% ($p < 0.01$) and TRAP expression decreased by 76.3% ($p < 0.01$) (Fig. 3C). Osteoclast activity is increased in patients with osteoporosis, and these mature osteoclasts with increased activity overexpress CTSK and TRAP. The degradation of inorganic minerals in an acidic microenvironment in the presence of excess H^+ allows these enzymes to rapidly degrade the organic components of bone tissue.[52] Our experiments suggest that Sr–Fe LDH likely can inhibit fusion and maturation of osteoclasts by down-regulating the gene expression of CTSK and TRAP, and also suggests that the material may be

able to reverse the phenomenon of bone resorption induced by increased osteoclast activity.

3.3 *In vivo* study

3.3.1 Establishment of the osteoporosis model. Osteoporosis in postmenopausal women is primarily caused by a decrease in ovarian function, which results in a significant decrease in estrogen secretion.[53–55] Numerous studies have demonstrated that bilateral ovariectomy can induce osteoporosis in rodents.[56] To demonstrate the effect of Sr–Fe LDH coating on osseointegration in an osteoporotic state *in vivo*, we first created an osteoporotic rat model by performing bilateral oophorectomy. Three-month-old female SD rats underwent bilateral ovariectomy, a model for 12 W was developed, and the control group consisted of female rats that underwent a sham operation. X-ray (Fig. S6A, ESI†) and micro-CT (Fig. S6B, ESI†) reconstructions revealed significant bone loss in ovariectomy-treated rodents. According to the quantitative analysis of the three-point bending test (Fig. S6C, ESI†). the elastic modulus of the tibia of rats undergoing ovariectomy was 49.2% lower than that of the sham operation group; micro-CT analysis (Fig. S6D–G, ESI†) revealed that the BV/TV of the tibial metaphyseal decreased by 39.0%, and the Tb. Sp increased by 33.4%. As osteoporosis leads to bone tissue loss, the macroscopic manifestation is the destruction of the bone microstructure. In micro-CT analysis of the tibia of rats with osteoporosis, a decrease in the number of trabeculae (Tb. N), bone volume
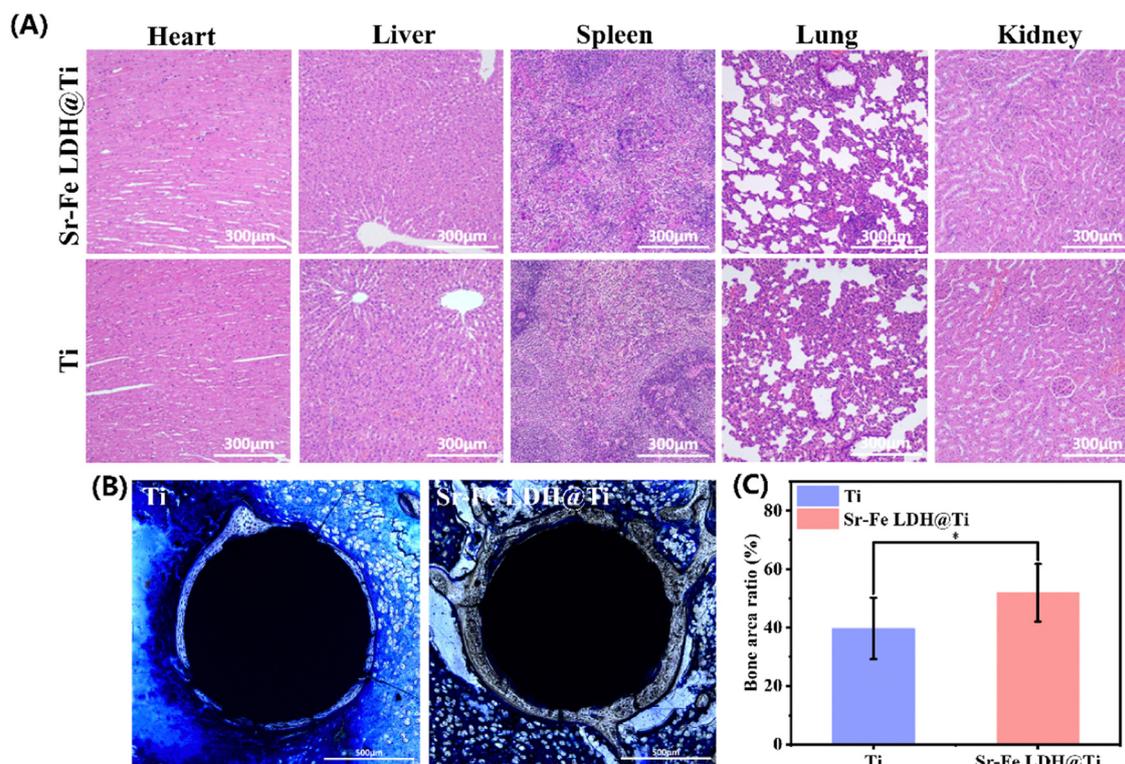

Fig. 5 (A) Hematoxylin eosin staining of the heart, liver, spleen, lungs, and kidneys in rats. (B) Histological images of the proximal tibiae with implants below the epiphyseal plate 8w after implantation; $n = 11$ and (C) result of the Bone area ratio analysis; $n = 11$. All values are presented as mean ± s.d. *$p < 0.05$, **$p < 0.01$, and ***$p < 0.001$.

1600 | *J. Mater. Chem. B*, 2024, **12**, 1592–1603

This journal is © The Royal Society of Chemistry 2024

fraction (BV/TV), and trabecular thickness (Tb. Th) and an increase in trabecular segregation (Tb. Sp) can be found.[57] A decrease in the elastic modulus of rat tibia can be found by biomechanical testing.[58] Therefore, our experimental results can prove that our rat osteoporosis model is established successfully.

3.3.2 Analysis of the biomechanical test and micro-CT. Analyzing the maximal push-out force on the implant during biomechanical tests[59] is an indirect method for determining the strength of the bond between the implant and the bone tissue. The push-out experiments revealed (Fig. 4A) that the maximum push-out force of Sr–Fe LDH in the tibia was substantially increased by 72.2% (p 0.01) compared to Ti. As the volume of interest (VOI) for the micro-CT experiments, we selected the tibia below the growth plate and within 500 m of the implant (Fig. 4B). By reconstructing the bone tissue around the implant, we were able to observe that the bone tissue grown on the surface of Sr–Fe LDH was denser than that on Ti (Fig. 4C). By quantitative analysis, we found a 12.4% ($p < 0.05$) increase in the number of trabeculae (Tb.N) (Fig. 4D), a 58.6% ($p < 0.05$) increase in the bone volume fraction (BV/TV) (Fig. 4E), and a 31.6% ($p < 0.01$) increase in the thickness of the trabeculae (Tb.Th) (Fig. 4F) in the bone tissue surrounding the Sr–Fe LDH@Ti as compared to the bone tissue surrounding the Ti.

3.3.3 Histological analysis. To determine the biosafety of the material *in vivo*, H&E staining was conducted on the major organs (heart, liver, spleen, lung, and kidney) of rats during the histological section experiment. No obvious organic damage was detected in the major organs of rats implanted with either Ti or Sr–Fe LDH 8 weeks after implantation. Biosafety *in vivo* can be demonstrated (Fig. 5A). Toluidine blue staining (Fig. 5B) and semi-quantitative analysis of the adjacent tissues (Fig. 5C) revealed that the percentage of the bone area surrounding Sr–Fe LDH was 30.9% greater than Ti ($p < 0.05$). The growth trend is consistent with micro-CT analysis results. These findings indicate that Sr–Fe LDH can substantially stimulate the regeneration of local bone tissue *in vivo* and can form a solid osseous integration.

4. Conclusions

To regulate the abnormal acidic microenvironment caused by osteoporosis, as well as to improve the dysfunctional state of osteoblasts and osteoclasts, the ultimate goal is to improve osseointegration. In this work, we combined the excellent performance of Sr^{2+} in improving bone metabolism and the ability of alkaline LDH to neutralize acids and prepared Sr–Fe LDH coatings on the surface of pure titanium implants by the hydrothermal method using Fe^{3+}, which has good biosafety. The alkaline Sr–Fe LDH coating has good acid neutralization capacity as well as the ability to release Sr^{2+} for a long and stable period, is biocompatible with osteoblasts and monocyte macrophages, and can inhibit osteoclast differentiation and maturation while promoting osteoblast proliferation and

differentiation. Mechanical stability, peripheral bone formation, and osseointegration of pure titanium implants in OVX rats were promoted by the modulation of the acidic microenvironment, as well as osteoblast and osteoclast functions. Our results demonstrate that the Sr–Fe LDH coating is a promising implant coating for patients with osteoporosis and has the potential to reduce instability, loosening, and dislodgement of implants in osteoporosis patients and to improve the success rate of implant placement surgery. In the next study, we will focus on the angiogenic and immunomodulatory ability of Sr–Fe LDH coating on osteoporotic rats.

Conflicts of interest

The authors declare that they have no known competing financial interests or personal relationships that could have appeared to influence the work reported in this paper.

Acknowledgements

References

1 I. R. Reid, *Nat. Rev. Endocrinol.*, 2020, **16**, 333–339.

2 W. D. Leslie and S. N. Morin, *Curr. Osteoporos. Rep.*, 2020, **18**, 115–129.

3 M. Fini, G. Giavaresi, T. Greggi, L. Martini, N. N. Aldini, P. Parisini and R. Giardino, *J. Biomed. Mater. Res., Part A*, 2003, **66A**, 176–183.

4 Y. Li, F. Li, C. C. Zhang, B. A. Gao, P. Tan, B. G. Mi, Y. Zhang, H. Cheng, H. Liao, K. F. Huo and W. Xiong, *J. Nanosci. Nanotechnol.*, 2015, **15**, 4136–4142.

5 Y. D. He, Y. X. Gao, Q. L. Ma, X. G. Zhang, Y. M. Zhang and W. Song, *J. Nanobiotechnol.*, 2022, **20**, 22.

6 Y. D. He, Z. Li, X. Ding, B. Y. Xu, J. J. Wang, Y. Li, F. H. Chen, F. H. Meng, W. Song and Y. M. Zhang, *Bioact. Mater.*, 2022, **8**, 109–123.

7 X. F. Lin, Q. Q. Wang, C. H. Gu, M. B. Li, K. Chen, P. F. Chen, Z. B. Tang, X. Liu, H. H. Pan, Z. M. Liu, R. K. Tang and S. W. Fan, *J. Am. Chem. Soc.*, 2020, **142**, 17543–17556.

8 J. E. Compston, M. R. McClung and W. D. Leslie, *Lancet*, 2019, **393**, 364–376.

This journal is © The Royal Society of Chemistry 2024

J. Mater. Chem. B, 2024, **12**, 1592–1603 | **1601**

9 Y. H. Shen, W. C. Liu, C. Y. Wen, H. B. Pan, T. Wang, B. W. Darvell, W. W. Lu and W. H. Huang, *J. Mater. Chem.*, 2012, **22**, 8662–8670.

10 L. Kyllonen, M. D'Este, M. Alini and D. Eglin, *Acta Biomater.*, 2015, **11**, 412–434.

11 J. K. Zhang, Y. Zhuang, R. L. Sheng, H. Tomás, J. Rodrigues, G. Y. Yuan, X. D. Wang and K. L. Lin, *Mater. Horiz.*, 2024, **11**, 12–36.

12 H. P. Wei, J. J. Cui, K. L. Lin, J. Xie and X. D. Wang, *Bone Res.*, 2022, **10**, 17.

13 M. U. Joshi, S. P. Kulkarni, M. Choppadandi, M. Keerthana and G. Kapusetti, *Smart Mater. Med.*, 2023, **4**, 661–679.

14 R. Agarwal and A. J. Garcia, *Adv. Drug Delivery Rev.*, 2015, **94**, 53–62.

15 T. Wang, J. X. Bai, M. Lu, C. L. Huang, D. C. Geng, G. Chen, L. Wang, J. Qi, W. G. Cui and L. F. Deng, *Nat. Commun.*, 2022, **13**, 17.

16 S. Song, G. H. Zhang, X. T. Chen, J. Zheng, X. D. Liu, Y. Q. Wang, Z. J. Chen, Y. X. Wang, Y. L. Song and Q. Zhou, *J. Nanobiotechnol.*, 2023, **21**, 257.

17 R. Smeets, B. Stadlinger, F. Schwarz, B. Beck-Broichsitter, O. Jung, C. Precht, F. Kloss, A. Grobe, M. Heiland and T. Ebker, *Biomed Res. Int.*, 2016, **2016**, 16.

18 E. Campodoni, M. Montanari, C. Artusi, G. Bassi, F. Furlani, M. Montesi, S. Panseri, M. Sandri and A. Tampieri, *J. Compos. Sci.*, 2021, **5**, 278.

19 M. Dermience, G. Lognay, F. Mathieu and P. Goyens, *J. Trace Elem. Med. Biol.*, 2015, **32**, 86–106.

20 Z. Ciosek, K. Kot, D. Kosik-Bogacka, N. Lanocha-Arendarczyk and I. Rotter, *Biomolecules*, 2021, **11**, 26.

21 E. O'Neill, G. Awale, L. Daneshmandi, O. Umerah and K. W. H. Lo, *Drug Discovery Today*, 2018, **23**, 879–890.

22 Z. S. Patel, S. Young, Y. Tabata, J. A. Jansen, M. E. K. Wong and A. G. Mikos, *Bone*, 2008, **43**, 931–940.

23 U. Bilati, E. Allemann and E. Doelker, *Eur. J. Pharm. Biopharm.*, 2005, **59**, 375–388.

24 P. Marquis, C. Roux, C. de la Loge, M. Diaz-Curiel, C. Cormier, G. Isaia, J. Badurski, J. Wark and P. J. Meunier, *Osteoporosis Int.*, 2008, **19**, 503–510.

25 R. Yan, J. H. Li, Q. J. Wu, X. K. Zhang, L. W. Hu, Y. W. Deng, R. X. Jiang, J. Wen and X. Q. Jiang, *Front. Chem.*, 2022, **10**, 16.

26 T. Y. Geng, Y. R. Wang, K. L. Lin, C. Zhang, J. Wang, Y. Liu, C. Y. Yuan and P. L. Wang, *Front. Bioeng. Biotechnol.*, 2022, **10**, 12.

27 C. Zhou, Z. Y. Ge, L. Song, J. H. Yan, X. R. Lang, Y. Z. Zhang and F. M. He, *Clin. Oral Implant. Res.*, 2023, **34**, 297–311.

28 M. R. Katunar, J. I. Pastore, A. Cisilino, J. Merlo, L. S. Alonso, M. Baca, K. Haddad, S. Cere and J. Ballarre, *Surf. Coat. Technol.*, 2022, **433**, 9.

29 Y. W. Ge, Z. H. Fan, Q. F. Ke, Y. P. Guo, C. Q. Zhang and W. T. Jia, *Mater. Today Bio*, 2022, **16**, 13.

30 D. D. Zhang, S. Cheng, J. Tan, J. N. Xie, Y. Zhang, S. H. Chen, H. H. Du, S. Qian, Y. Q. Qiao, F. Peng and X. Y. Liu, *Bioact. Mater.*, 2022, **17**, 394–405.

31 D. D. Cao, Z. L. Xu, Y. X. Chen, Q. F. Ke, C. Q. Zhang and Y. P. Guo, *J. Biomed. Mater. Res., Part B*, 2018, **106**, 863–873.

32 Q. W. Li, D. H. Wang, J. J. Qiu, F. Peng and X. Y. Liu, *Biomater. Sci.*, 2018, **6**, 1227–1237.

33 T. T. Hu, Z. Gu, G. R. Williams, M. Strimaite, J. J. Zha, Z. Zhou, X. C. Zhang, C. L. Tan and R. Z. Liang, *Chem. Soc. Rev.*, 2022, **51**, 6126–6176.

34 H. Fu, L. T. Wang, Q. Q. Bao, D. L. Ni, P. Hu and J. L. Shi, *J. Am. Chem. Soc.*, 2022, **144**, 8987–8999.

35 M. M. Bornstein, P. Valderrama, A. A. Jones, T. G. Wilson, R. Seibl and D. L. Cochran, *Clin. Oral Implant. Res.*, 2008, **19**, 233–241.

36 C. Eriksson, H. Nygren and K. Ohlson, *Biomaterials*, 2004, **25**, 4759–4766.

37 Z. Y. Zhong, X. D. Wu, Y. F. Wang, M. D. Li, Y. Li, X. L. Liu, X. Zhang, Z. Y. Lan, J. L. Wang, Y. Y. Du and S. M. Zhang, *Bioact. Mater.*, 2022, **10**, 195–206.

38 C. B. Tovani, T. M. Oliveira, M. P. R. Soares, N. Nassif, S. Y. Fukada, P. Ciancaglini, A. Gloter and A. P. Ramos, *ACS Appl. Mater. Interfaces*, 2020, **12**, 43422–43434.

39 D. L. Kendler, F. Marin, C. A. F. Zerbini, L. A. Russo, S. L. Greenspan, V. Zikan, A. Bagur, J. Malouf-Sierra, P. Lakatos, A. Fahrleitner-Pammer, E. Lespessailles, S. Minisola, J. J. Body, P. Geusens, R. Möricke and P. López-Romero, *Lancet*, 2018, **391**, 230–240.

40 D. M. Biskobing and D. Fan, *Calcif. Tissue Int.*, 2000, **67**, 178–183.

41 N. Udagawa, J. Takito and T. Suda, *Nihon rinsho*, 1992, **50**, 2133–2138.

42 S. J. Jenkins, D. Ruckerl, P. C. Cook, L. H. Jones, F. D. Finkelman, N. van Rooijen, A. S. MacDonald and J. E. Allen, *Science*, 2011, **332**, 1284–1288.

43 M. A. Kafi, K. Aktar, Y. Phanny and M. Todo, *J. Mater. Sci.-Mater. Med.*, 2019, **30**, 131.

44 M. Kingsak, P. Maturavongsadit, H. Jiang and Q. Wang, *Biomater. Transl.*, 2022, **3**, 221–233.

45 M. Chu, Z. Y. Sun, Z. H. Fan, D. G. Yu, Y. Q. Mao and Y. P. Guo, *Theranostics*, 2021, **11**, 6717–6734.

46 Y. J. Wang, X. Mei, Y. Y. Bian, T. T. Hu, X. S. Weng, R. Z. Liang and M. Wei, *Nanoscale*, 2020, **12**, 19075–19082.

47 J. F. Li, L. Yang, X. D. Guo, W. Cui, S. Y. Yang, J. P. Wang, Y. Z. Qu, Z. W. Shao and S. Y. Xu, *Biomed. Mater.*, 2018, **13**, 13.

48 Y. Z. Zhu, H. Liang, X. M. Liu, J. Wu, C. Yang, T. M. Wong, K. Y. H. Kwan, K. M. C. Cheung, S. L. Wu and K. W. K. Yeung, *Sci. Adv.*, 2021, **7**, 13.

49 Z. C. Cao, H. M. Wang, J. L. Chen, Y. A. Zhang, Q. Y. Mo, P. Zhang, M. Y. Wang, H. Y. Liu, X. Y. Bao, Y. Z. Sun, W. Zhang and Q. Q. Yao, *Bioact. Mater.*, 2023, **20**, 221–242.

50 J. H. Hwang, Y. S. Park, H. S. Kim, K. Dong-ha, S. H. Lee, C. H. Lee, S. H. Lee, J. E. Kim, S. Lee, H. M. Kim, H. W. Kim, J. Kim, W. Seo, H. J. Kwon, B. J. Song, D. K. Kim, M. C. Baek and Y. E. Cho, *J. Controlled Release*, 2023, **355**, 184–198.

51 Y. H. Shen, W. C. Liu, K. L. Lin, H. B. Pan, B. W. Darvell, S. L. Peng, C. Y. Wen, L. F. Deng, W. W. Lu and J. A. Chang, *Langmuir*, 2011, **27**, 2701–2708.

52 K. Chen, P. C. Qiu, Y. Yuan, L. Zheng, J. B. He, C. Wang, Q. Guo, J. Kenny, Q. Liu, J. M. Zhao, J. H. Chen, J. Tickner,

1602 | *J. Mater. Chem. B*, 2024, **12**, 1592–1603

This journal is © The Royal Society of Chemistry 2024

S. W. Fan, X. F. Lin and J. K. Xu, *Theranostics*, 2019, **9**, 1634–1650.

53 C. L. Gregson, D. J. Armstrong, J. Bowden, C. Cooper, J. Edwards, N. J. L. Gittoes, N. Harvey, J. Kanis, S. Leyland, R. Low, E. McCloskey, K. Moss, J. Parker, Z. Paskins, K. Poole, D. M. Reid, M. Stone, J. Thomson, N. Vine and J. Compston, *Arch. Osteoporos.*, 2022, **17**, 46.

54 F. Cosman, S. J. de Beur, M. S. LeBoff, E. M. Lewiecki, B. Tanner, S. Randall and R. Lindsay, *Osteoporosis Int.*, 2014, **25**, 2359–2381.

55 C. B. Johnston and M. Dagar, *Med. Clin. N. Am.*, 2020, **104**, 873–884.

56 N. Yousefzadeh, K. Kashfi, S. Jeddi and A. Ghasemi, *Excli J.*, 2020, **19**, 89–107.

57 O. Barou, D. Valentin, L. Vico, C. Tirode, A. Barbier, C. Alexandre and M. H. Lafage-Proust, *Invest. Radiol.*, 2002, **37**, 40–46.

58 L. Maïmoun, T. C. Brennan-Speranza, R. Rizzoli and P. Ammann, *Bone*, 2012, **51**, 586–591.

59 Y. F. Li, Q. Li, S. S. Zhu, E. Luo, J. H. Li, G. Feng, Y. M. Liao and J. Hu, *Biomaterials*, 2010, **31**, 9006–9014.

This journal is © The Royal Society of Chemistry 2024

J. Mater. Chem. B, 2024, **12**, 1592–1603 | **1603**